Chinese Chemical Letters 34 (2023) 107378

Contents lists available at ScienceDirect

Chinese Chemical Letters

journal homepage: www.elsevier.com/locate/cclet

Tailoring the electronic acceptor–donor heterointerface between black phosphorus and Co_3O_4 for boosting oxygen bifunctional electrocatalysis

Jing Zou[a], Yilun Zou[a], Haitao Wang[a,*], Wei Wang[c], Pingxiu Wu[d], Arramel[e], Jizhou Jiang[a,b,*], Xin Li[f,*]

[a] School of Chemistry and Environmental Engineering, School of Environmental Ecology and Biological Engineering, Key Laboratory of Green Chemical Engineering Process of Ministry of Education, Engineering Research Center of Phosphorus Resources Development and Utilization of Ministry of Education, Hubei Tree Gorges Laboratory, Wuhan Institute of Technology, Wuhan 430205, China
[b] Key Laboratory of Rare Mineral, Ministry of Natural Resources, Geological Experimental Testing Center of Hubei Province, Wuhan 430034, China
[c] Key Laboratory of Hunan Province for Advanced Carbon-based Functional Materials, Hunan Institute of Science and Technology, Yueyang 414006, China
[d] Semiconductor Electronic Special Gas of Hubei Engineering Research Center, Jingzhou 434000, China
[e] Nano Center Indonesia, Jl. PUSPIPTEK Tangerang Selatan, Banten 15314, Indonesia
[f] Institute of Biomass Engineering, Key Laboratory of Energy Plants Resource and Utilization, Ministry of Agriculture and Rural Affairs, South China Agricultural University, Guangzhou 510642, China

ARTICLE INFO

Article history:
Received 27 December 2021
Revised 29 January 2022
Accepted 25 March 2022
Available online 28 March 2022

Keywords:
Electronic acceptor-donor
Black phosphorus
Co_3O_4
Charge transfer
Oxygen bifunctional electrocatalysis

ABSTRACT

Black phosphorus (BP) as an uprising two-dimensional material exhibits attractive potential in the field of electrocatalysis due to the inherent advantages of high carrier mobility and abundant lone pair electrons. However, the exposed active electrons compel BP to be deactivated by oxidative degradation. Herein, the electronic signature of acceptor-donor heterointerfacial interactions between BP and Co_3O_4 is realized *via* wet ball milling. The preferential migration of active electrons from BP to Co_3O_4 is achieved at the heterointerface since the Fermi level of BP is higher than that of Co_3O_4. Such relative energetic consideration promotes reasonable oxygen electrocatalytic active sites. Moreover, it significantly suppresses the oxidative degradation of BP. Consequently, the resulting Co_3O_4/BP heterojunction possesses superior oxygen bifunctional electrocatalytic activity than its parent catalysts. Most importantly, this work promotes an efficient route towards BP-based multifunctional catalysts.

Oxygen evolution reaction (OER) and oxygen reduction reaction (ORR) are of importance to determine the overall performance of various electrochemical energy conversion technologies such as water splittings, fuel cells and rechargeable metal-air cells [1–3]. However, the kinetics that governing these mechanisms are impeded by their low energy conversion efficiency [4]. For example, we note that noble metals-based electrocatalysts in the case of Pt/C, RuO_2 and IrO_2, hold as competitive OER or ORR catalysts. However, these materials are quite scarce which restrict their widespread usage [5]. To this end, the employment of earth-abundant materials, including transition metal oxides, phosphides, hydroxides, sulfides and nitrides, are economically-feasible as an attractive strategy to tackle this hindrance [6–9]. Unfortunately, simple single of them normally exhibt dissatisfied oxygen bifunctional electrocatalytic activity, since the poor electrical conductivity, inactivated catalytic active sites and limited electron transfer rate. Therefore, the construction of heterostructure electrocatalysts comprised of different active components is urgently needed for acquiring the efficient oxygen bifunctional electrocatalytic performance.

Black phosphorus (BP) as an up-rising member of two-dimensional (2D) graphene-like materials has aroused soaring interest in optical and electronic applications since the first report in 2014, owing to its appealing advantages, such as the unique anisotropic properties, high carrier mobility and puckered-honeycomb configuration [10–12]. Particularly, the abundance of active lone pair electrons in BP supply favorable chemisorption sites for the oxygen-related molecules or ions, endowing BP as a potential oxygen electrocatalyst [13,14]. Ideally, these lone pair electrons exposed to the surface of ultrathin BP all can be served

* Corresponding authors.
E-mail addresses: wanghaitao@wit.edu.cn (H. Wang), 027wit@163.com (J. Jiang), xinli@scau.edu.cn (X. Li).

https://doi.org/10.1016/j.cclet.2022.03.101
1001-8417/

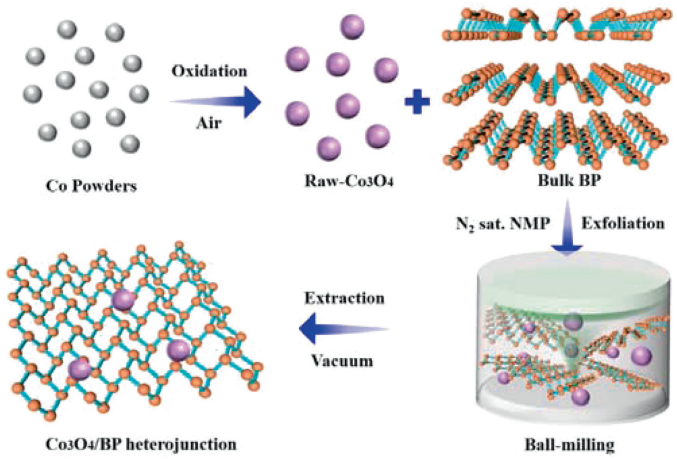

Fig. 1. Schematic demonstration of the formation of Co_3O_4/BP.

as oxygen electrocatalytic active sites [15]. However, the presence of rich lone pair electrons makes BP extremely vulnerable to oxidative degradation, especially in strong oxidation and high anodic potential environment towards OER catalytic processes [16]. To date, the common strategies to stabilize BP is either to passivate the exposed lone pairs electrons by coating the BP NSs with various protective materials, which inevitably weakens the intrinsic electrocatalytic activity of BP [17,18]. Therefore, developing an effective strategy to take advantage of those active electrons to achieve electronic structural innovation is highly desirable for enhancing the OER electrocatalytic activity and stability. Additionally, exploiting an excellent BP-based oxygen bifunctional electrocatalyst toward OER and ORR remains as an emergent challenge that needs to be tackled.

Encouraged by these findings, herein, we construct a unique electronic acceptor-donor heterointerfacial interaction between BP and Co_3O_4 (Co_3O_4/BP heterojunction) through wet ball milling process. The intensive Co_3O_4/BP heterointerfacial interaction is disclosed explicitly by the formation of Co–O–P and Co–P bonds over the Co_3O_4/BP between BP and adjacent Co_3O_4. Consequently, the active electrons exposed on the surface of BP will migrate to Co_3O_4 since the higher Fermi level of BP compared with that of Co_3O_4. Such charge transfer not only impedes the oxidative deterioration of BP effectively, but also convert partially Co^{3+} to the oxygen electrocatalytic active species of Co^{2+}, thus donating the improvement of oxygen bifunctional electrocatalysis.

Typically, the synthesis process of Co_3O_4/BP heterojunction can be designed *via* wet ball-milling (Fig. 1, experimental details are shown in Supporting information). Firstly, the Raw-Co_3O_4 is prepared by a universal oxidation treatment (Fig. S2a in Supporting information) of commercial Co powders (particle size: around 400 nm, Fig. S1a in Supporting information). Subsequently, the formed Raw-Co_3O_4 (particle size: around 850 nm, Fig. S1b in Supporting information) and Bulk-BP are ultrasonic dispersed in N_2-saturated NMP (*N*-methyl-2-pyrrolidone). Finally, the Co_3O_4/BP heterojunction is developed by wet ball-milling under N_2 protection.

X-ray diffraction (XRD) patterns displayed in Fig. 2a clarify the crystalline nature as-grown samples. The distinct diffraction peaks located at the approximately of 16.8°, 26.7°, 34.1°, 34.9°, 52.4°and 56.1° correspond to the (020), (021), (040), (111), (060) and (151) diffraction planes of BP. While the additional peaks centered in 31.3°, 36.9°, 59.4° and 65.2° are attributed to the (220), (311), (511) and (440) reflections of crystalline Co_3O_4, which demonstrates the successful formation of Co_3O_4/BP heterojunction. Noticeably, the almost disappeared (021) diffraction peaks of Co_3O_4/BP can be ascribed to the reduction of BP crystallinity and the facilitation of BP lamellar exfoliation during the Co_3O_4-coexisting ball milling, which is consistent with the results previously reported [19,20]. In addition, the identical diffraction peak positions observed in Figs. S2b and c (Supporting information) reveal the unchanged crystalline nature of Co_3O_4 and BP after ball-milling with N_2-saturated NMP. Therein, the obviously weakened peak intensity after wet ball milling can be attributed to the reduction in the size of Co_3O_4 and BP.

Fig. 2b presents a typical transmission electron microscopy (TEM) image of BP, where the lattice spacing of 0.26 nm is indexed to (040) facets of BP, which is consistent with the discrete spots from the selected-area electron diffraction (SAED) presented in the inset. Moreover, the well-defined two-dimensional (2D) lamellar morphology demonstrates a definitive conversion of BP from the blocks (Fig. S3 in Supporting information) to nanosheets (Fig. S4 in Supporting information). Fig. 2c and Fig. S5 (Supporting information) show the TEM and scanning electron microscopy (SEM) images of Co_3O_4/BP heterojunction, which not only display flake-like nanostructure, but also reveal a fair amount of Co_3O_4 nanoparticles with a diameter of about 40 nm embedded in the lamellate BP skeleton. Moreover, the main discrete spots observed in corresponding SAED pattern match well with the structures of BP and Co_3O_4. The topographic detail of Co_3O_4/BP heterojunction is further probed by atomic force microscope (AFM, Fig. 2d), which gives a thickness of ~17 nm for BP nanosheets and a diameter of ~38 nm for Co_3O_4 nanoparticles. The elemental composition and distribution of Co_3O_4/BP heterojunction is investigated by energy dispersive X-ray spectroscopy (EDX) measurements. The corresponding element mappings in Fig. 2e demonstrate the coexistence of P, Co and O elements over the Co_3O_4/BP sample. Moreover, the mapping patterns of Co incorporated with the same domain of O signal reveals the successful construction of Co_3O_4/BP heterojunction. The specific surface area and pore properties of Co_3O_4/BP are investigated by recording the corresponding N_2 sorption isotherms (Fig. 2f). Noteworthy, the surface area and average pore size of the Co_3O_4/BP are calculated to be 15.39 m^2/g and 6.37 nm, which are larger than those of Co_3O_4 and BP (Fig. S6 and Table S1 in Supporting information). Such considerable improvement on the surface area and porosity are highly anticipated since these features provide rich active sites and high electron transfer rates, thereby heightening the oxygen bifunctional catalysis [21,22].

Fig. 2g exemplifies a typical high-resolution TEM (HRTEM) image of heterointerface between Co_3O_4 and BP, in which the interplanar lattice spacing of 0.26 nm is indexed to the (440) facet of orthorhombic BP (Fig. 2h), while the lattice distance of 0.29 and 0.23 nm are attributed to the (220) and (311) planes of cubic Co_3O_4 (Fig. 2h and Fig. S7 in Supporting information). Moreover, we found that Co_3O_4 are well connected with several BP layers. Interestingly, the unique microscopic configuration of heterointerface not only induces the interfacial electron transfer between Co_3O_4 and adjacent BP, but also inhibits the agglomeration and dissolution of Co_3O_4 nanoparticles, thus resulting in the improvement of oxygen catalytic activity and stability.

Raman spectroscopy is employed to examine the heterointerfacial interaction of Co_3O_4/BP. Fig. 2i compares the Raman spectra of BP, Co_3O_4 and Co_3O_4/BP samples, where the three peaks located at around 462, 438 and 467 cm^{-1} belong to the A_{1g} out-of-plane, B_{2g} armchair and A_{2g} zig-zag vibrational modes of BP, respectively [23,24]. Besides, the remainder signals centered at 469 and 673 cm^{-1} associated to the E_g tetrahedral site (Co^{2+}) and A_{1g} octahedral site (Co^{3+}) vibrational modes of Co_3O_4 [25]. Notably, the positions of such characteristic vibration peaks observed in Co_3O_4/BP are shifted to lower and higher wavenumbers with respect to the pristine BP and Co_3O_4, indicating the existence of intimate heterointerface interactions between different constituents

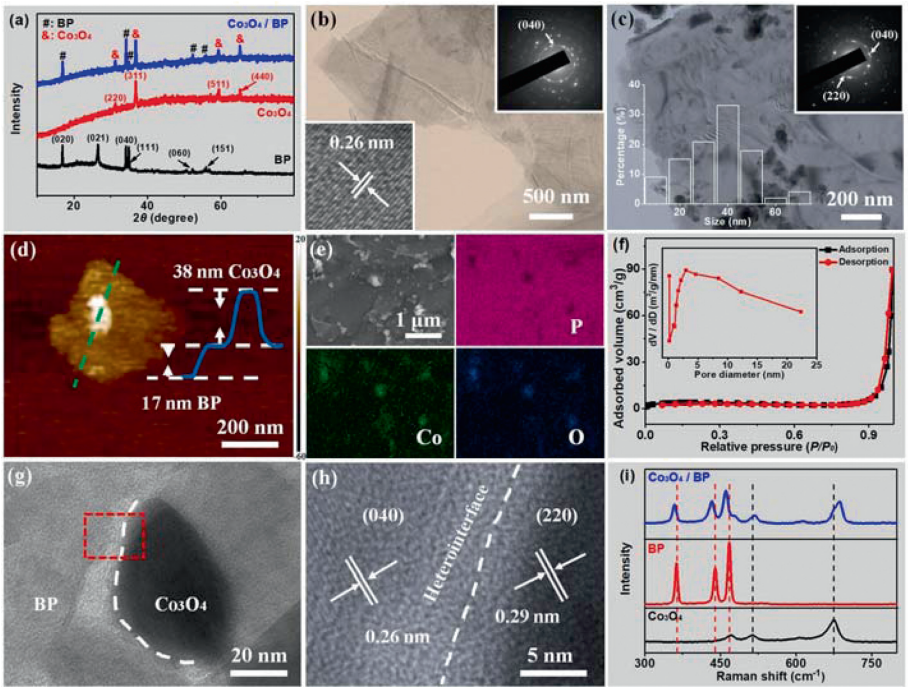

Fig. 2. (a) XRD patterns of BP, Co_3O_4 and Co_3O_4/BP. (b) TEM images and SAED patterns of BP and (c) Co_3O_4/BP (inset is the histogram of Co_3O_4 particle size distributions). (d) AFM image and (e) EDX element mappings of Co_3O_4/BP. (f) N_2 sorption isotherms and the corresponding pore size distribution of Co_3O4/BP. (g, h) HRTEM images of Co_3O_4/BP. (i) Raman spectra of BP, Co_3O_4 and Co_3O_4/BP.

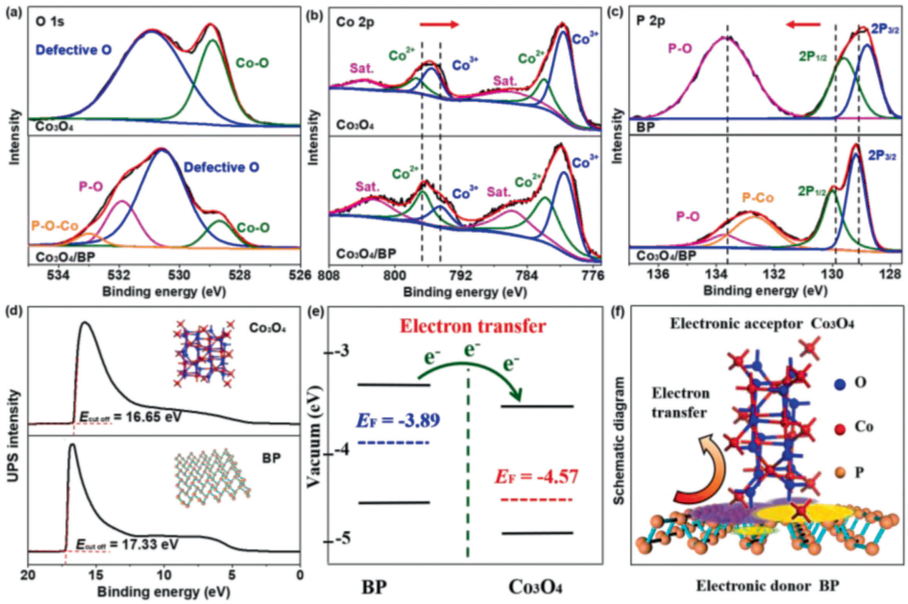

Fig. 3. High-resolution XPS spectra of (a) O 1s, (b) Co 2p, and (c) P 2p for the Co_3O_4, BP or Co_3O_4/BP. (d) UPS spectra and (e) the corresponding energy band diagram of Co_3O_4 and BP. (f) Schematic diagram of the electron transfer in Co_3O_4/BP heterointerfaces, where the violet and yellow isosurfaces depict the heterointerfacial interaction.

in the Co_3O_4/BP heterojunction [26]. In order to clarify the essence of such interaction, the zeta potentials of BP, Co_3O_4 and Co_3O_4/BP are initial recorded as presented in Fig. S8 (Supporting information). The opposite charge distributions of BP and Co_3O_4 resulted intensive electronic interactions at the heterointerface, which is conducive to the electronic transmission between BP and Co_3O_4.

Accordingly, the electronic states and interactions of the surface elemental configuration for the Co_3O_4/BP heterojunction are further explored by X-ray photoelectron spectroscopy (XPS) technique (Tables S2 and S3 in Supporting information). Fig. 3a and Fig. S9 (Supporting information) reveal the high-resolution XPS spectra of O 1s for the Co_3O_4, BP and Co_3O_4/BP samples, in which the obvious peak at ~528.5 eV corresponds to the Co–O bond of Co_3O_4 [27], while other peak which was observed at ~530.4 eV originates from low-coordinated defects of oxygen, and the located at 531.6 eV attributes to the P–O bond of BP [28]. Remarkably, an additional signal is detected significantly at ~533.0 eV towards Co_3O_4/BP, which can be assigned to the P–O–Co bond coupling by the oxygenic functional groups of Co_3O_4 and BP [29], resembling that of C–O-Ni and C–O–Co reported earlier [30,31]. The formed P-

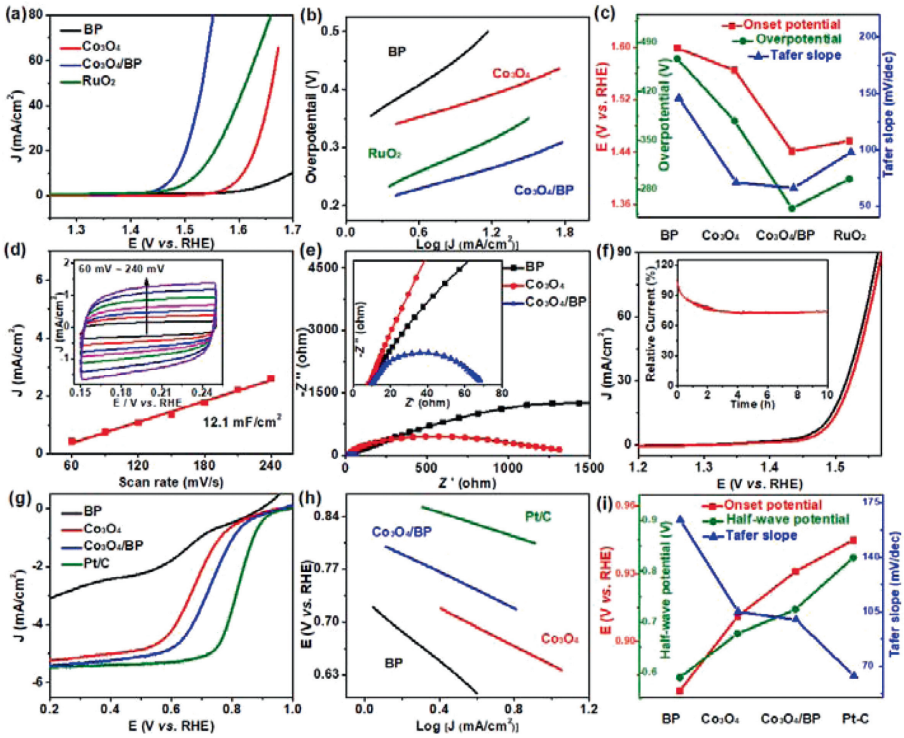

Fig. 4. (a) LSVs, (b) Tafel plots and (c) the corresponding Tafel slopes, E_0 and η_{10} of BP, Co_3O_4, Co_3O_4/BP and RuO_2 towards OER. (d) CVs and the calculated C_{dl} of Co_3O_4/BP. (e) EIS plots of BP, Co_3O_4 and Co_3O_4/BP. (f) LSVs of Co_3O_4/BP before and after 1000 repetitive cycles, as well as the chronoamperometric response towards OER. (g) LSVs, (h) Tafel plots and (i) the corresponding calculated Tafel slopes, E_0 and $E_{1/2}$ of BP, Co_3O_4, Co_3O_4/BP and Pt/C towards ORR.

O-Co bond strongly suggests the forceful coupling between 2D BP nanosheets and Co_3O_4 nanoparticles.

Fig. 3b displays the high-resolution Co 2p spectra of Co_3O_4 and Co_3O_4/BP, where the peaks centered at 779.4 and 794.5 eV confirm the existence of Co^{3+} species, while the signals detected at 781.7 and 796.6 eV reveal the presence of Co^{2+} in the crystalline Co_3O_4 [27]. Meanwhile, the high-resolution P 2p spectra of BP and Co_3O_4/BP are also deconvoluted in Fig. 3c. Therein, the prominent peaks located at 129.2, 130.0 and 133.7 eV are assigned to the $2p_{3/2}$, $2p_{1/2}$ and P–O species, respectively [32]. In particular, the peak that appeared at the binding energy of 132.7 eV indicated the chemical bonding between P and Co, confirming the intense electron affinity of BP to Co [33]. Additionally, such an obvious electronic interaction is also proved by comparing the Co 2p and P 2p binding energies of Co_3O_4/BP with those of BP or Co_3O_4. Generally, the positive shift of binding energy indicates the attenuated electronic screening effect due to the decrease of the electron density, whereas the corresponding negative shift suggests an enhanced electron density [19]. Notably, the negative and positive binding energies shifts of Co 2p and P 2p observed in Figs. 3b and c demonstrate an increase and decrease in the electron density of Co and BP over the Co_3O_4/BP heterojunction. In other words, electrons tend to transfer from BP to Co_3O_4 through the Co/BP heterointerface (Fig. 2h) after the formation of Co_3O_4/BP heterojunction. It is worth mentioning that the P–O signal was reduced explicitly in the high-resolution P 2p spectrum of Co_3O_4/BP (Fig. 3c), which suggests the electron transfer from BP to Co effectively inhibits the oxidative degradation of BP, thereby improving the oxygen electrocatalytic stability.

In addition, the ultraviolet photoelectron spectra (UPS) are recorded at the excitation energy of 21.22 eV (He I. *vs.* the vacuum level) to evaluate the direction of electron transfer between BP and Co_3O_4 catalytic active sites (Fig. 3d). The work functions of BP and Co_3O_4 are calculated by subtracting the electron cut-off energy, which stands for the difference between the vacuum level (0 eV) and Fermi level (E_f) [34]. Consequently, the E_f of BP and Co_3O_4 are found to be −3.89 and −4.57 eV (Fig. 3e). Therefore, to reach E_f equilibrium, the electron will migrate from BP to Co_3O_4 (Fig. 3f), which is in accordance well with the XPS results. We propose such effective electron migrations not only create massive oxygen electrocatalytic active sites of Co^{2+} in Co_3O_4, but also this effort protect BP from oxidative degradation, hence improving the oxygen electrocatalytic properties.

The OER electrocatalytic properties are assessed firstly by linear sweep voltammetries (LSVs). Before further analyses, the mass ratio between Bulk-BP and Raw-Co_3O_4 (P/Co) is optimized (Fig. S10 in Supporting information). Noted that the superordinate onset potential (E_0) and prominent overpotential at the current density of 10 mA/cm^2 (η_{10}) reveal the best electrochemical performance of Co_3O_4/BP obtained at the P/Co of 2/5 (Experimental section in Supporting information). Fig. 4a compares the LSVs of BP, Co_3O_4, Co_3O_4/BP in O_2-saturated 1.0 mol/L KOH, while employs RuO_2 as a benchmark. Remarkably, the Co_3O_4/BP heterojunction possesses the most positive E_0 (1.448 V) and lowest η_{10} (253 mV) in comparison to those of BP and Co_3O_4 (Table S4 in Supporting information), and even exceeded than RuO_2, confirming the excellent OER catalytic activity of Co_3O_4/BP. Moreover, to the best of our knowledge, the OER catalytic activity of Co_3O_4/BP is one of the highest photocatalytic activities for other BP-based catalysts recently reported (Table S5 in Supporting information). Such an outstanding catalytic performance can be further verified by contrasting the corresponding Tafel slopes (Fig. 4b). Co_3O_4/BP heterojunction exhibits a Tafel slope of 68 mV/dec (Fig. 4c), which is slightly smaller than RuO_2, highlighting a more favorable OER kinetics of Co_3O_4/BP. The electrochemical impedance spectroscopy (EIS) and double-layer capacitance (C_{dl}) tests are carried out to evaluate the electron transfer efficiency and electrochemical active surface area (ECSA). Figs. 4d and e and Fig. S11 (Supporting information) show the results of

C_{dl} and EIS measurements, in which the smallest nyquist semicircle and largest C_{dl} imply the lowest electron transfer resistance and highest intrinsic oxygen electrocatalytic activity of the Co_3O_4/BP heterojunction compared with those of single-catalysts (BP and Co_3O_4). In addition to catalytic activity, the durability is also necessary for an excellent oxygen catalyst. Fig. 4f exhibit the LSVs and chronoamperometric response of Co_3O_4/BP, in which the attenuations of E_0 and η_{10} for the Co_3O_4/BP are almost negligible after 1000 continuous OER cycles. Moreover, the loss of current density for the Co_3O_4/BP is only around 24% after 10 h continuous OER operation (Fig. S12a in Supporting information), confirming the robust durability of developed Co_3O_4/BP heterojunction. The HRTEM image after the repetitive cycles reveals that Co_3O_4 nanoparticles still well dispersed on the lamellar BP substance, again demonstrating its good structure stability (Fig. S13 in Supporting information). The high-resolution XPS spectra of Co 2p and P 2p of Co_3O_4/BP before and after OER cycles so as to clarify the OER process (Fig. S14 and Table S6 in Supporting information). The shift towards lower binding energies of Co $2P_{1/2}$ and Co $2P_{3/2}$ indicates the oxidation process of Co^{2+} to Co^{3+}, which also can be confirmed by the increased atomic ratio of Co^{3+}/Co^{2+} after OER test (Tables S3 and S6 in Supporting information). Such results suggest that the low valent Co ions in Co_3O_4 provides the actual active sites for OER electrocatalysis. Additionally, the negligible increase in the P-O ratio from 11.8% to 19.4% results from the slight oxidation of BP during the OER process.

Considering of the structural and electronic characterizations, the Co_3O_4/BP heterojunction possesses outstanding OER catalytic activity and stability, which can be attributed to the following several critical aspects. The first consideration is the high carrier mobility of BP endows high electrical conductivity of Co_3O_4/BP, thereby enhancing the electronic transmission rate. Secondly, the emblematic laminar nanoskeleton accompanied by rich porosity enhances the transport efficiency of OER-related reactants, intermediates and products [35]. Thirdly, the preferential transfer of active electron from BP to Co_3O_4 effective inhibits the oxidative degradation of BP active substance, thus ensuring the excellent OER durability of Co_3O_4/BP (Figs. S12a and b in Supporting information). Most importantly, the intensive heterointerfacial coupling between BP and Co_3O_4 *via* the formation of Co–P bonds endows a unique electronic acceptor-donor interaction, which compels partial Co^{3+} to be reduced to the highly-active sites of divalent Co^{2+}, further resulting in the vastly promotion of OER electrocatalysis [29]. The significant role of heterointerface in boosting the OER catalytic performance can also be highlighted by comparing the LSVs of Co_3O_4+BP (direct mixing of Co_3O_4 and BP) and Co_3O_4/BP heterojunction. As presented in Figs. S12c and S15 (Supporting information), in the absence of interfacial electron interaction, a poorer OER activity and stability is observed over the Co_3O_4+BP sample, which unambiguously indicate the indispensability of heterointerface in the OER electrocatalysis.

Motivated by the beneficial heterointerfacial coupling between BP and Co_3O_4, the ORR catalytic activities of BP, Co_3O_4 and Co_3O_4/BP are evaluated additionally in O_2-saturated 0.1 mol/L KOH, while Pt/C catalyst is benchmarked. Notably, the tendency of the ORR activity is in agreement well with that of OER (Figs. 4a and g). The Co_3O_4/BP heterojunction possesses the optimum ORR electrocatalytic activity in terms of the most positive E_0 and half-wave potential ($E_{1/2}$) in comparison with those of single BP and Co_3O_4 (Table S7 in Supporting information), even the catalytic performance is comparable to the Pt/C reference catalyst. The corresponding Tafel plots are further analyzed to investigate the ORR catalytic kinetics (Fig. 4h). We confirm Co_3O_4/BP heterojunction display a Tafel slope of 98 mV/dec (Fig. 4i), which is close to that of Pt/C, suggesting an equally efficient ORR kinetic process of Co_3O_4/BP as Pt/C. The Co_3O_4/BP displays enhanced ORR catalytic activity than that of the substrate can be attributed to the high electrical conductivity of Co_3O_4/BP and the intensive heterointerfacial coupling between BP and Co_3O_4, leading to the accelerated electron transport. Moreover, the afforded Co_3O_4/BP catalyst also exhibits a satisfactory ORR durability with a slight loss of activity after 6000 continuous ORR cycles (Fig. S16 in Supporting information). The above results persuasively reveal that the afforded Co_3O_4/BP heterojunction is a promising oxygen bifunctional catalyst.

In conclusion, a compact heterointerface between Co_3O_4 and BP has been elaborately constructed by wet ball-milling to boost the oxygen bifunctional electrocatalytic performance. The developed Co_3O_4/BP heterojunction possesses a discernible two-dimensional lamellar morphology with abundant porosity. Moreover, the formation of Co–O–P and Co–P bonds over the Co_3O_4/BP heterojunction reflect an intensive junction between BP and Co_3O_4. In particular, such heterointerface provides a unique electronic acceptor-donor interaction between Co_3O_4 and BP. Therein, due to higher Fermi level position of BP than that of Co_3O_4, facilitating the effective electrons transfer from BP to Co_3O_4. This energetically suppress the oxidative degradation of BP, and partially convert the Co^{3+} to its reduced active sites of divalent Co^{2+}. Therefore, the explored Co_3O_4/BP heterojunction exhibits superior oxygen bifunctional electrocatalytic properties compared to the BP and Co_3O_4 catalysts. Importantly, by constructing the Co_3O_4/BP heterointerface provides a referential strategy to design highly active BP-based oxygen bifunctional catalysts.

Declaration of competing interest

The authors declare that they have no known competing financial interests or personal relationships that could have appeared to influence the work reported in this paper.

Acknowledgments

This work was supported by the National Natural Science Foundation of China (No. 62004143), the Natural Science Foundation of Hubei Province (No. 2021CFB133), the Central Government Guided Local Science and Technology Development Special Fund Project (No. 2020ZYYD033), the Opening Fund of Key Laboratory of Rare Mineral,Ministry of Natural Resources (No. KLRM-KF 202005), the Innovation Project of Engineering Research Center of Phosphorus Resources Development and Utilization of Ministry of Education (No. LCX2021003), the Open Research Fund of Key Laboratory of Material Chemistry for Energy Conversion and Storage (HUST), Ministry of Education (No. 2021JYBKF05), the Opening Fund of Key Laboratory for Green Chemical Process of Ministry of Education of Wuhan Institute of Technology (No. GCP202101), and the 13th Graduate Education Innovation Fund of Wuhan Institute of Technology. This work is dedicated to celebrating the 50th anniversary of Wuhan Institute of Technology.

Supplementary materials

Supplementary material associated with this article can be found, in the online version, at doi:10.1016/j.cclet.2022.03.101.

References

[1] F. Wang, J. Tseng, Z. Liu, et al., Adv. Mater. 32 (2020) 2000287.
[2] X. Zhao, H. Zhang, Y. Yan, et al., Angew. Chem. Int. Ed. 56 (2017) 328–332.
[3] Z. Li, X. Wu, X. Jiang, et al., Adv. Powder Mater. 1 (2022) 100020.
[4] X. Zhao, X. Li, Y. Yan, et al., Appl. Catal. B 236 (2018) 569–575.
[5] D. He, X. Wu, W. Liu, et al., Chin. Chem. Lett. 30 (2019) 229–233.
[6] B. Deng, J. Liang, L. Yue, et al., Chin. Chem. Lett. 33 (2022) 890–892.
[7] G. Zhao, W. Ma, X. Wang, et al., Adv. Powder Mater. 1 (2022) 100008.
[8] X.P. Li, C. Huang, W.K. Han, et al., Chin. Chem. Lett. 32 (2021) 2597–2616.

[9] F. Chen, Z. Zhang, W. Liang, et al., Chin. Chem. Lett. 33 (2022) 1395–1402.
[10] P. Li, J. Lu, H. Cui, et al., Mater. Adv. 2 (2021) 2483–2509.
[11] W. Gao, Y. Zhou, X. Wu, et al., Adv. Funct. Mater. 31 (2021) 2005197.
[12] J. Cheng, L. Gao, T. Li, et al., Nano-Micro Lett. 12 (2020) 179.
[13] H. Qiao, H. Liu, Z. Huang, et al., Adv. Energy Mater. 10 (2020) 2002424.
[14] J. Wang, D. Liu, H. Huang, et al., Angew. Chem. Int. Ed. 130 (2018) 2630–2634.
[15] L. Zhang, L.X. Ding, G.F. Chen, et al., Angew. Chem. Int. Ed. 58 (2019) 2612–2616.
[16] X. Zhu, T. Zhang, D. Jiang, et al., Nat. Commun. 9 (2018) 4177.
[17] X. Liu, K. Chen, X. Li, et al., Adv. Mater. 33 (2021) 2005924.
[18] Y. Zhang, C.Y. Ma, J.L. Xie, et al., Adv. Mater. 33 (2021) 2100113.
[19] F. Shi, Z. Geng, K. Huang, et al., Adv. Sci. 5 (2018) 1800575.
[20] H. Xiao, X. Du, M. Zhao, et al., Nanoscale 13 (2021) 7381–7388.
[21] Y. Li, Q. Guo, Y. Jiang, et al., Chin. Chem. Lett. 32 (2021) 755–760.
[22] R. Zhong, C. Zhi, Y. Wu, et al., Chin. Chem. Lett. 31 (2020) 1588–1592.
[23] X. Chen, J. Zhang, C. Huang, et al., ACS Appl. Mater. Interfaces 12 (2020) 54619–54626.
[24] W. Lu, H. Nan, J. Hong, et al., Nano Res. 7 (2014) 853–859.
[25] S.H. Hsu, S.F. Hung, H.Y. Wang, et al., Small Methods 2 (2018) 1800001.
[26] R. He, J. Hua, A. Zhang, et al., Nano Lett. 17 (2017) 4311–4316.
[27] L. Xu, Q. Jiang, Z. Xiao, et al., Angew. Chem. Int. Ed. 55 (2016) 5277–5281.
[28] M. Zhu, X. Cai, M. Fujitsuka, et al., Angew. Chem. Int. Ed. 56 (2017) 2064–2068.
[29] F. Shi, K. Huang, Y. Wang, et al., ACS Appl. Mater. Interfaces 11 (2019) 17459–17466.
[30] G. Zhou, D.W. Wang, L.C. Yin, et al., ACS Nano 6 (2012) 3214–3223.
[31] Y. Dou, J. Xu, B. Ruan, et al., Adv. Energy Mater. 6 (2016) 1501835.
[32] D. Hanlon, C. Backes, E. Doherty, et al., Nat. Commun. 6 (2015) 8563.
[33] X. Li, L. Xiao, L. Zhou, et al., Angew. Chem. Int. Ed. 59 (2020) 21106–21113.
[34] S. Guo, Y. Li, C. Xue, et al., Chem. Eng. J. 419 (2021) 129213.
[35] H. Jing, P. Zhu, X. Zheng, et al., Adv. Powder Mater. 1 (2022) 100013.